Version: Preprint

1 **A Combinatorial Investigation of Fe-Si-Zn Thin Film Negative Electrodes for Li-ion**
2 **Batteries**
3

4 L. MacEachern[a], R.A. Dunlap[a,b,c] and M.N. Obrovac [a,b,d,]*

5

6 a - Department of Physics and Atmospheric Science, Dalhousie University,
7 P.O. Box 15000, Halifax, Nova Scotia. B3H 4R2 Canada
8 b - Institute for Research in Materials, Dalhousie University, P.O. Box 15000,
9 Halifax, Nova Scotia, B3H 4R2 Canada
10 c - College of Sustainability, Dalhousie University, P.O. Box 15000, Halifax,
11 Nova Scotia B3H 4R2 Canada
12 d - Department of Chemistry, Dalhousie University, Dalhousie University,
13 P.O. Box 15000, Halifax, Nova Scotia B3H 4R2 Canada
14 * - corresponding author: mnobrovac@dal.ca

15

16 **Abstract**

17 Thin-film Fe-Si-Zn libraries were investigated as negative electrode materials for Li-ion

18 batteries using combinatorial and high-throughput techniques. X-ray diffraction and electron

19 microprobe measurements were used to characterize the library structure. A large amorphous

20 region exists in Si-rich compositions of this system. The electrochemistry of numerous

21 compositions of Fe-Si-Zn materials was determined near room temperature. Both Zn and Fe

22 additions to Si were found to suppress the formation of $Li_{15}Si_4$ during cycling.

23

24 **Introduction**

25 Silicon-based negative electrode materials are of interest for use in Li-ion rechargeable

26 batteries due to their high volumetric capacity and low average voltage. Si has a theoretical

27 capacity of 2190 Ah/L. Pure Si negative electrodes have been studied in detail,[1–6] but due to

28 their high volume expansion at full lithiation (~280%) their cycleability is poor when cycled to

29 full capacity. It has been shown that the cycleability of pure crystalline Si electrodes can be

30 significantly improved by cycling to a limited capacity and keeping the lower cutoff voltage

31 above 170 mV.[5] Cycling of Si can also be improved by adding elements that suppress formation

32 of $Li_{15}Si_4$, such as Zn, Ag, and Sn, or by reducing volume expansion by adding an inactive

33 phase, such as Fe.[7–10] Numerous Si-containing alloy negative electrode materials have been

34 studied, including, but not limited to; Si-Sn,[9] Si-C,[11] Si-Fe,[10,12] Si-TiN-C,[11] Si-Zn-C,[13] Si-Al-

35 Sn,[14] Si-Al-Mn,[15] and Si-Sn-C.[16]

36   Improvement in cell performance can be obtained by incorporating elements that do not

37 alloy with Li into alloy electrodes. Adding an inactive phase to the electrode dilutes the volume

38 expansion, improves cycle life, and increases energy density at a given volume expansion due to

39 lower average voltage compared to pure Si cycled to limited capacity.[17] Fleischauer *et al.*

40 showed that increasing Mn concentration in Si-Al-Mn thin-film electrodes improved capacity

41 retention, but total specific capacity decreased with increasing Mn.[15] Dong *et al.* found that

42 $Fe_{0.25}Si_{0.75}$ electrodes exhibited reduced initial capacity, but better cycleability and higher

43 coulombic efficiency (CE) compared to pure Si electrodes.[12]

44   Elements that are active with Li, but with lower specific capacity (and lower volume

45 expansion) than Si have also been shown to improve cycling performance of alloy negative

46 electrodes. These elements suppress formation of $Li_{15}Si_4$ formation, avoiding two-phase regions

47 and high internal stresses during cycling. Zn, Ag, and Sn have all been found to improve cycling

48 for this reason.[18] Zn alloys with Li in a 1:1 ratio and has a theoretical capacity of 410 mAh/g.

49 Hatchard *et al*. found that Si-Zn thin film electrodes with approximate composition of $Si_{0.4}Zn_{0.6}$

50   had reversible capacities over 1000 mAh/g and cycled quite well.[7] In-situ X-Ray Diffraction

51   (XRD) experiments were used to show that Si-Zn electrodes become amorphous during cycling.

52   Electrodes with greater than 20% content suppressed the formation of $Li_{15}Si_4$ during cycling.

53   Yoon *et al.* reported good cycling performance for mechanically milled Si-Zn-C composite

54   electrodes.[13] They found that 91% of the initial discharge capacity could be retained for 40

55   cycles.

56   The binary systems of Si-Fe, Si-Zn, and Fe-Zn have been previously tested as negative

57   electrode materials for Li-ion batteries.[7,10,19] Increasing concentration of Fe and Zn in Fe-Si and

58   Si-Zn alloys, respectively, has been reported to improve cycling performance in Li-ion battery

59   negative electrodes.[7,10,12,19] Fleischauer *et al.* studied the electrochemistry of Si_xFe_{1-x} thin films

60   and found that capacity decreased nearly linearly from pure Si to 60 atom % Si.[10] They found

61   that capacity can be predicted nicely when Si_xFe_{1-x} is assumed to comprise $(2x - 1)$ Si and $(2 -$

62    $2x)$ inactive Si-Fe for $0.5 < x < 1$. The addition of Fe has also been reported to improve cycling

63   performance in Fe-Zn alloy negative electrodes.[20] Sputtered Fe_xZn_{1-x} libraries have recently

64   been studied in detail by MacEachern *et al.*.[19] The capacity of Fe_xZn_{1-x} electrodes was found to

65   decrease linearly with increasing Fe content up to $x = 0.12$ where capacity dropped sharply to

66   zero. Capacities for $x < 0.12$ can be predicted well assuming each additional Fe atom renders

67   two Zn atoms inactive. Ex-situ Mössbauer studies of cycled $Fe_{0.08}Zn_{0.92}$ electrodes suggested

68   that during lithiation Fe was displaced from the alloy, resulting in formation of LiZn, inactive δ-

69   phase Fe-Zn, and isolated Fe. Coulombic efficiencies and capacity retention were improved with

70   increasing Fe concentration, although no compositions showed good overall performance.[19]

71   Here, the structure and electrochemistry of the Fe-Si-Zn thin-film system is studied. This

72   system is predicted to comprise three phases: an inactive FeSi phase, an active pure Si phase and

73   an active pure Zn phase, based on the ternary phase diagram and previous electrochemical

74   measurements done on the Fe-Si binary system.[21,22] In studying this system it was hoped that the

75   advantages of the Si-Fe system (lower volume expansion) and the Si-Zn system (suppression of

76     $Li_{15}Si_4$ formation) could be combined to result in high performance anode materials.

77

78   **Experimental**

79   Thin film libraries were produced using a Corona Vacuum Coated model V3-T sputtering

80   system. A base pressure of $< 4\times10^{-7}$Torr was obtained by evacuating the vacuum chamber using

81   a Varian 500 L/s turbo pump backed by a roughing pump. Ar gas was used to maintain the

82   pressure at 1 mTorr during sputter deposition. Three types of 5.08 cm diameter targets were

83   used on four of the five available magnetrons: one Zn target (99.99% purity, Kurt J. Lester

84   Company), two Si targets (99.99% purity, Williams Advanced Materials), and one Fe target

85   (produced by stacking two 50 mm diameter disks cut from 0.7 mm thick sheets of grade 1008

86   low carbon steel). A chrome plasma scrubber electrode was mounted on the fifth magnetron.

87   Library composition was made to vary in a linear and orthogonal manner by using

88   different stationary masks over the targets. Constant masks were used for the Si targets, and

89   linear out masks were used for the Fe and Zn targets. The sputtering table was rotated at 15 rpm

90   to ensure sufficient atomic level mixing during sputtering. In this way, four libraries were

91   sputtered to obtain a range of compositions and to test for reproducibility. The libraries had

92   constant Si content, while the Fe and Zn content varied orthogonally over the library. The details

93   of the combinatorial sputtering system have been described by Dahn *et al.*[23] and the techniques

94   used to obtain ternary libraries have been presented by Fleischauer *et al.*[24] Various substrates

95   were placed on the sputtering table for characterization of the deposited thin film libraries. A 5×

96   5 grid of copper foil disks were used to determine the mass of the deposited film and were also

97   used as electrodes in electrochemical coin cells. A silicon (100) wafer was used for X-ray

98   diffraction measurements and a copper coated glass plate was used for electron microprobe

99   composition analysis of the libraries.

100   The position dependence of the mass was found by weighing the Cu disks on a Sartorious

101   SE-2 microbalance (0.1 μg precision) before and after sputter deposition. The films had mass

102   loadings of 0.25 - 1.56 mg/cm^2 and calculated thickness between 0.80 - 5.71 μm, depending on

103   the library. Mass loading and calculated thickness for individual libraries is given in Table 1.

104   Compositions as a function of position within the libraries was determined with a JEOL-8200

105   Superprobe electron microprobe using wavelength dispersive spectroscopy on an 8 × 8 grid of

106   points over the sputtered library. X-ray diffraction (XRD) measurements were also obtained on

107   an 8 × 8 grid of points over the sputtered library using a Bruker D8 Discover X-ray

108   diffractometer equipped with a Cu target and a Cu-K$_\alpha$ monochromator. The X-ray beam was

109   incident on the sample at an angle of 6°, which does not satisfy the Bragg condition for Si; as a

110   result, the Si wafer acts as a zero background holder.

111   Electrodes deposited on Cu disks 1.26 cm^2 in area were incorporated into 2325 coin cells

112   with Li metal counter electrodes and 1 M LiPF$_6$ in ethylene carbonate (EC) / ethyl methyl

113   carbonate (EMC) / fluoroethylene carbonate (FEC) in a 2/7/1 v/v/v ratio for library Spt101 and 1

114   M LiPF$_6$ in EC/DEC/FEC 3:6:1 v/v/v electrolyte for library Spt107 (all from BASF, < 50 ppm

115   H$_2$O). The electrodes were separated with two layers of Celgard 2301 separator. All cell

116   assembly was performed in an Ar-filled glove box. Cells were cycled at 30°C with a Maccor

117   Series 4000 Automated Test System from 0.005 V to 1.2 V at a C/10 rate and trickled until a

118   C/20 rate was reached at the lower voltage limit during discharge (lithiation). The C rate was

119   calculated assuming that three phases are present in the sputtered film: FeSi, Si, and Zn and that

120   the FeSi phase is inactive, the remaining Si alloys with 3.75 Li per Si, and all the Zn present is

121   active and alloys with 1 Li per Zn.

122

123   **Results and Discussion**

124   Table 1 gives a summary of powers supplied to targets during sputtering and composition

125   ranges obtained for each run. All libraries were sputtered for 4 hours. Figure 1 shows the range

126   of Fe-Si-Zn compositions fabricated in a single sputtering run (Spt107). The labeled points

127   correspond to plots in Figure 2 which shows the X-Ray diffraction (XRD) patterns for library

128   Spt107. Figure 3 shows XRD patterns for the bottom row of Figure 2. The Zn concentration is

129   approximately constant along this row (~29 at%) and the Fe concentration increases from 4 at%

130   to 21 at%, while the Si concentration decreases from 67 to 50 at%.

131   It is clear from Figures 2 and 3 that the Zn microstructure in the film is dependent not

132   only on Zn concentration, but also on the Fe and Si concentration. Si-Zn thin films can be

133   sputtered amorphously for compositions with less than 45 at% Zn,[7] which agrees well with the

134   results found in this work for the lowest Fe concentrations. Si-Fe thin films can be sputtered

135   amorphously for compositions with less than 72 at% Fe.[25] The range of compositions fabricated

136   in this work did not extend above 50 at% Fe and all compositions along the Si-Fe portion of the

137   phase diagram were found to be amorphous, agreeing with previously reported results.[25] Along

138   lines of constant Zn composition, crystalline Zn formation becomes more favorable when both

139   Fe and Si are present. Crystalline Zn peaks begin to appear in the XRD patterns when the Zn

140   concentration is above 25 at% in compositions with a 4:1 Si:Fe ratio. Figure 4 shows a summary

141   of the structures determined by XRD for all Fe-Si-Zn libraries presented in this work. The entire

142   shaded region in the figure indicates the total range of compositions while the darker shaded

143   region corresponds to the range of Fe-Si-Zn compositions that can be sputtered amorphously.

144   Figure 5 shows compositions on the Fe-Si-Zn Gibbs' Triangle for which electrochemical

145   studies are presented. The electrochemical results presented are for coin cells with electrodes

146   from library Spt101. Electrochemical measurements were also conducted using coin cells with

147   electrodes from library Spt107 and the results were consistent with those obtained from library

148   Spt101. Figure 6 correlates the electrodes used in coin cells prepared from library Spt101 with

149   the XRD patterns obtained from library Spt101.

150   Voltage curves for the first 1.5 cycles for Spt101 are shown in Figure 7. Voltage curves

151   for all compositions show long sloping plateaus, characteristic of amorphous materials. Two

152   distinct plateaus can be seen for voltage curves in the Si rich region (see plot 5 in Figure 7),

153   characteristic of amorphous Si.[1] As Zn and Fe concentrations in the electrode increase, these

154   plateaus become less defined. This can be seen more clearly in the differential capacity plots for

155   cells from library Spt101, shown in Figure 8. All plots show broad peaks during charge for the

156   first two cycles, indicating that the films remain amorphous during the first two cycles. The

157   peaks become less defined as Fe and Zn concentrations in the film increase. All electrodes

158   remain amorphous on cycling except those shown in panels 4 and 5 (electrodes with the highest

159   Si concentration), which show a sharp peak during charge for cycles 6-7 which is consistent with

160   the formation of $Li_{15}Si_4$.[3] Hatchard *et al.* concluded than a sufficient amount of Zn in Si-Zn thin

161   film electrodes suppressed the formation of the $Li_{15}Si_4$ phase.[7] In the present work, both Fe and

162   Zn appear to suppress $Li_{15}Si_4$ formation. The Zn and Fe concentrations required to suppress

163    $Li_{15}Si_4$ formation are 13 at% and 15 at%, respectively. Only electrodes containing the lowest Zn

164   and Fe concentrations showed evidence of $Li_{15}Si_4$ formation during cycling.

165   During the lithiation of Si-Zn thin films a ternary $Li_{2+x}SiZn$ phase is formed. During

166   delithiation, Zn does not phase separate and the films become amorphous or nanocrystalline.

167   This mechanism was thought to suppress Si phase aggregation during cycling and, as a result,

168   also suppress $Li_{15}Si_4$ formation.[7] It is possible that the FeSi inactive phase may also suppress Si

169   aggregation in Si-Fe alloys, resulting in the suppression of $Li_{15}Si_4$ formation.   However,

170   additional mechanisms may be operating that suppress $Li_{15}Si_4$ in these films, as will be discuss

171   below.

172   Average discharge and charge voltages for all compositions are between 0.11 V - 0.17 V

173   and 0.37 V - 0.42 V, respectively. Average charge and discharge voltages were calculated for

174   the first charge and second discharge. The average discharge voltage decreases with increasing

175   Fe concentration and the average charge voltage increases with increasing Zn concentration.

176   Thus, hysteresis in the voltage curves increases as Fe and Zn concentrations are increased

177   concurrently in the electrode. This is illustrated in Figure 9 which shows an overlay of three

178   normalized voltage curves for the most Si rich ($Si_{0.86}Zn_{0.08}Fe_{0.06}$), Zn rich ($Si_{0.66}Zn_{0.29}Fe_{0.05}$), and

179   Fe rich ($Si_{0.74}Zn_{0.06}Fe_{0.20}$) compositions in library Spt101. For the most Fe rich composition the

180   charge portion of the voltage curve is identical to the most Si rich composition, and the discharge

181   portion of the curve is at a lower voltage. Although Fe depresses the voltage of the discharge

182   voltage curve, the features in the discharge voltage curve remain unchanged. For the most Zn

183   rich composition the discharge portion of the voltage curve is identical to the most Si rich

184   composition, and the charge portion of the curve is at a higher voltage.

185   Variation in average voltage can also be seen in the differential capacity plots shown in

186   Figure 8. Fe concentration is increasing from right (panel 5) to left (panel 1) along the top row

187   of Figure 8. Positions of the discharge peaks near 0.09 V and 0.26 V shift to lower voltage as Fe

188   concentration is increased, decreasing the average discharge voltage. Zn concentration is

189   increasing from top (panel 5) to bottom (panel 25) in the rightmost column of Figure 8. As Zn

190   concentration is increased a broad peak on charge is introduced at 0.74 V, increasing the average

191   charge voltage. This high voltage peak has been previously observed in Si-Zn thin films.

192   Contour plots of average discharge (a) and average charge voltage (b) versus composition are

193   overlaid on a portion of the Fe-Si-Zn Gibbs' triangle in Figure 10. Surprisingly, the average

194   discharge voltage is a function of Fe content only (increasing Fe concentration decreases the

195   discharge voltage) and the average charge voltage is a function of Zn content only (increasing Zn

196   concentration increases the charge voltage).

197   The effect of the depression of the discharge voltage curve with increasing Fe content has

198   not been previously reported, although it can be readily seen in the differential capacity plots

199   shown in the study of all of the sputtered Si-M alloy systems (M = Fe, Mn, (Ni + Cr)) by

200   Fleischauer et al.[10] We do not know the origin of this discharge voltage depression. Whatever

201   its cause, the depression in the voltage curve is as much as 0.75 V. Since $Li_{15}Si_4$ formation

202   occurs below 50 mV in pure Si,[2] the voltage depression caused by the addition of transition

203   metals is likely the cause of the suppression of $Li_{15}Si_4$ formation in Si-M alloys.

204   The initial coulombic efficiency (ICE) of the Fe-Si-Zn alloys varied from 0.80 (cell 10)

205   to 0.94 (cell 24). The ICE showed a linear dependence on Si concentration in the electrode. ICE

206   versus Si concentration is shown in Figure 11 for coin cells prepared from libraries Spt101 and

207   Spt107. A line of best fit determined by least squares is shown. Anomalous points were not

208   included in the fit. A contour plot of predicted and observed first charge capacities for cells from

209   library Spt101 is shown in Figure 12. Capacities of cells are predicted assuming all Fe is in an

210   inactive FeSi 1:1 phase, the remaining Si alloys with 3.75 Li per Si, and all Zn present is active

211   and alloys with 1 Li per Zn. Predicted capacities agree well with the observed capacities,

212   indicating that the thin-films comprise inactive FeSi, active Si, and active Zn.

213

214   **Conclusions**

215   Thin film libraries of Fe-Si-Zn were fabricated and characterized using combinatorial

216   high throughput techniques. A large range of Fe-Si-Zn compositions can be sputtered

217   amorphously near the Si-rich corner of the phase diagram. The voltage curves and capacities of

218   the films was strongly dependent on composition. Fe and Zn additions to Si were both found to

219   decrease capacity, but both also suppressed $Li_{15}Si_4$ formation during cycling. The mechanism by

220   which Zn suppresses Si formation has been previously studied. Here it was found that Fe

221   additions to Si causes a significant depression in the discharge voltage curve without changing its

222   shape. This depression in the voltage curve likely contributes to the suppression of $Li_{15}Si_4$

223   formation during cycling in Si-M active/inactive alloys in general.

224   Initial coulombic efficiencies up to 0.94 were observed. Initial coulombic efficiency and

225   hysteresis improved with increasing Si concentration in the electrodes. Capacities were

226   predicted assuming that only three phases were present in the electrodes: FeSi, Si, and Zn.

227   Observed capacities agreed well with predicted capacities for all compositions..

228   This work shows that a wide composition range of amorphous Fe-Si-Zn thin-film

229   materials can be fabricated and compositions with sufficient Fe and Zn content remain

230   amorphous on electrochemical cycling. Further work needs to be done to understand the

231   electrochemistry of Fe-Si-Zn materials, especially the effect of discharge voltage depression

232   caused by the addition of Fe. Preparation of these materials using bulk methods is underway to

233   determine electrochemical properties in conventional electrode coatings.

234

Acknowledgements

241

242

243

244

245

246

247

248

249

250

References

252   1.   T.D. Hatchard, J.R. Dahn, *Journal of The Electrochemical Society*, **151** (6), A838 (2004).

253   2.   M.N. Obrovac, L. Christensen, *Electrochemical and Solid-State Letters*, **7** (5), A93
254   (2004).

255   3.   J. Li, J.R. Dahn, *Journal of The Electrochemical Society*, **154** (3), A156 (2007).

256   4.   U. Kasavajjula, C. Wang, A. J. Appleby, *Journal of Power Sources*, **163** (2), 1003 (2007).

257   5.   M.N. Obrovac, L.J. Krause, *Journal of The Electrochemical Society*, **154** (2), A103
258   (2007).

259   6.   K.L. Lee, J.Y. Jung, S.W. Lee, H.S. Moon, J.W. Park, *Journal of Power Sources*, **129** (2),
260   270 (2004).

261   7.   T.D. Hatchard, M.N. Obrovac, J.R. Dahn, *Journal of The Electrochemical Society*, **152**
262   (12), A2335 (2005).

263   8.   T.D. Hatchard, J.R. Dahn, *Journal of The Electrochemical Society*, **152** (7), A1445
264   (2005).

265   9.   T.D. Hatchard, J.R. Dahn, *Journal of The Electrochemical Society*, **151** (10), A1628
266   (2004).

267   10.   M.D. Fleischauer, J.M. Topple, J.R. Dahn, *Electrochemical and Solid-State Letters*, **8** (2),
268   A137 (2005).

269   11.   K. Hanai, Y. Liu, N. Imanishi, A. Hirano, M. Matsumura, T. Ichikawa, Y. Takeda,
270   *Journal of Power Sources*, **146** (1-2), 156 (2005).

271   12.   H. Dong, R.X. Feng, X.P. Ai, Y.L. Cao, H.X. Yang, *Electrochimica Acta*, **49** (28), 5217
272   (2004).

273   13.   S. Yoon, C.M. Park, H. Kim, H.J. Sohn, *Journal of Power Sources*, **167** (2), 520 (2007).

274   14.   T.D. Hatchard, J.M. Topple, M.D. Fleischauer, J.R. Dahn, *Electrochemical and Solid-*
275   *State Letters*, **6** (7), A129 (2003).

276   15.   M.D. Fleischauer, J.R. Dahn, *Journal of The Electrochemical Society*, **151** (8), A1216
277   (2004).

278   16.   M.A. Al-Maghrabi, J.S. Thorne, R.J. Sanderson, J.N. Byers, J.R. Dahn, R.A. Dunlap,
279   *Journal of The Electrochemical Society*, **159** (6), A711 (2012).

280   17.   M.N. Obrovac, L. Christensen, D.B. Le, J.R. Dahn, *Journal of The Electrochemical*
281   *Society*, **154** (9), A849 (2007).

282 18. T.D. Hatchard, M.N. Obrovac, J.R. Dahn, *Journal of The Electrochemical Society*, **153**
283   (2), A282 (2006).

284 19. L. MacEachern, M.N. Obrovac, R.A. Dunlap, Fe-Zn Negative Electrodes for Li-Ion
285   Batteries, (2014).

286 20. T. Fujieda, S. Takahashi, S. Higuchi, *Journal of Power Sources*, **40** (3), 283 (1992).

287 21. P. Villars, A. Prince, H. Okamoto, Handbook of Ternary Alloy Phase Diagrams, ASM
288   International, Materials Park, OH, (1995).

289 22. M.D. Fleischauer, M.N. Obrovac, J.D. McGraw, R.A. Dunlap, J.M. Topple, J.R. Dahn,
290   *Journal of The Electrochemical Society*, **153** (3), A484 (2006).

291 23. J.R. Dahn, S. Trussler, T.D. Hatchard, A. Bonakdarpour, J.R. Mueller-Neuhaus, K.C.
292   Hewitt, M. Fleischauer, *Chemistry of Materials*, **14** (8), 3519 (2002).

293 24. M.D. Fleischauer, T.D. Hatchard, A. Bonakdarpour, J.R. Dahn, *Measurement Science and*
294   *Technology*, **16** (1), 212 (2005).

295 25. J.D. McGraw, M.D. Fleischauer, J.R. Dahn, R.A. Dunlap, *Philosophical Magazine*, **86**
296   (32), 5017 (2006).

297 26. S.P. Ong, W.D. Richards, A. Jain, G. Hautier, M. Kocher, S. Cholia, D. Gunter, V.L.
298   Chevrier, K. A. Persson, G. Ceder, *Computational Materials Science*, **68**, 314 (2013).

299 27. A. Jain, S.P. Ong, G. Hautier, W. Chen, W.D. Richards, S. Dacek, S. Cholia, D. Gunter,
300   D. Skinner, G. Ceder, K. A. Persson, *APL Materials*, **1** (1), 011002 (2013).

301

302

303 **Table 1**

304

	Power Supplied to Targets			Film Composition		Mass Loading (mg/cm^2)	Calculated Thickness (µm)	Electrochemistry Y/N
Run ID	Si (W)	Fe (W)	Zn (W)	Fe (at%)	Zn (at%)			
Spt074	130 (×2)	110	25	$0.04 < x < 0.46$	$0.03 < y < 0.56$	0.68 - 1.56	1.99 - 5.71	N
Spt094	130 (×2)	85	17	$0.08 < x < 0.56$	$0.02 < y < 0.38$	0.38 - 0.87	1.02 - 2.39	N
Spt101	130 (×2)	33	13	$0.02 < x < 0.24$	$0.02 < y < 0.34$	0.31 - 0.58	0.95 - 1.80	Y
Spt107	125 (×2)	32	13	$0.02 < x < 0.23$	$0.02 < y < 0.31$	0.25 - 0.46	0.80 - 1.50	Y

305
306

307   Table 1 Summary of sputtered libraries presented in this work.

308

309

310

311

312

313

314

315

316

317

318

319

320

321

322   **Figure Captions**

323   **Figure 1: :** The Fe-Si-Zn ternary system as predicted by the Materials Project at 0 K.[26,27]   The

324   composition range of one sputtered library (Spt107) is superimposed on the diagram.   Numbers

325   correspond to XRD patterns shown in Figure 2.

326

327   **Figure 2:** XRD patterns of library Spt107. Positions of Zn peaks are indicated with triangles

328   (Δ). Numbers in top right corner of each plot correspond to compositions shown in Figure 1.

329

330   **Figure 3:** XRD patterns of compositions with constant Zn and varying Fe concentration from

331   Figure 2 (approximately corresponding to compositions in the range of $Fe_ySi_{1-y-0.29}Zn_{0.29}$; $0 < y <$

332   0.2). Zn peaks are indicated with triangles (Δ). The arrow points in the direction of increasing

333   Fe concentration.

334

335   **Figure 4:** Range of compositions sputtered in this work superimposed on the Fe-Si-Zn ternary

336   system as predicted by the Materials Project at 0 K.[26,27]   The entire shaded region represents

337   compositions fabricated in all four libraries.   The dark shaded region represents those

338   compositions which can be sputtered amorphously.

339

340   **Figure 5:** Compositions of coin cells prepared from library Spt101 superimposed on the Fe-Si-

341   Zn ternary system as predicted by the Materials Project at 0 K.[26,27] Numbers correspond to plots

342   in Figures 6, 7, 10, and 12.

343

344   **Figure 6:** Position of coin cells from library Spt101 overlaid onto XRD patterns obtained from

345   library Spt101. Zn peaks are indicated with triangles (Δ).

346

347   **Figure 7:** Voltage versus capacity cures for cells from library Spt101. Numbers in the top right

348   corner correspond to numbers shown on coin cells in Figure 6.

349

350   **Figure 8:** Differential capacity curves for cells prepared from library Spt101. The first two

351   cycles are shown in black and the sixth and seventh cycles are shown in red.

352

353   **Figure 9:** Overlay of voltage curves from panels 1, 5, and 25 in Figure 7. Capacity is

354   normalized by first discharge capacity.

355

356   **Figure 10:** Contour plot of average discharge voltage (a) and average charge voltage (b) of the

357   second cycle for cells in Figure 7. Average voltage values in volts are indicated on contour lines.

358   Cell compositions are shown in grey.

359

360   **Figure 11:** Initial coulombic efficiency as a function of Si concentration in the electrode for cells

361   prepared from libraries Spt101 (closed diamonds) and Spt107 (open diamonds). A line of best fit

362   by least squares is shown.

363

364   **Figure 12:** Contour plot of predicted (solid black lines) and observed (dashed red lines) capacity

365   for cells prepared from library Spt101 overlaid on a portion of the Fe-Si-Zn Gibbs' triangle.

366   Capacity values in mAh/g are indicated on contour lines. Cell compositions are shown in grey.

367

369
370
371
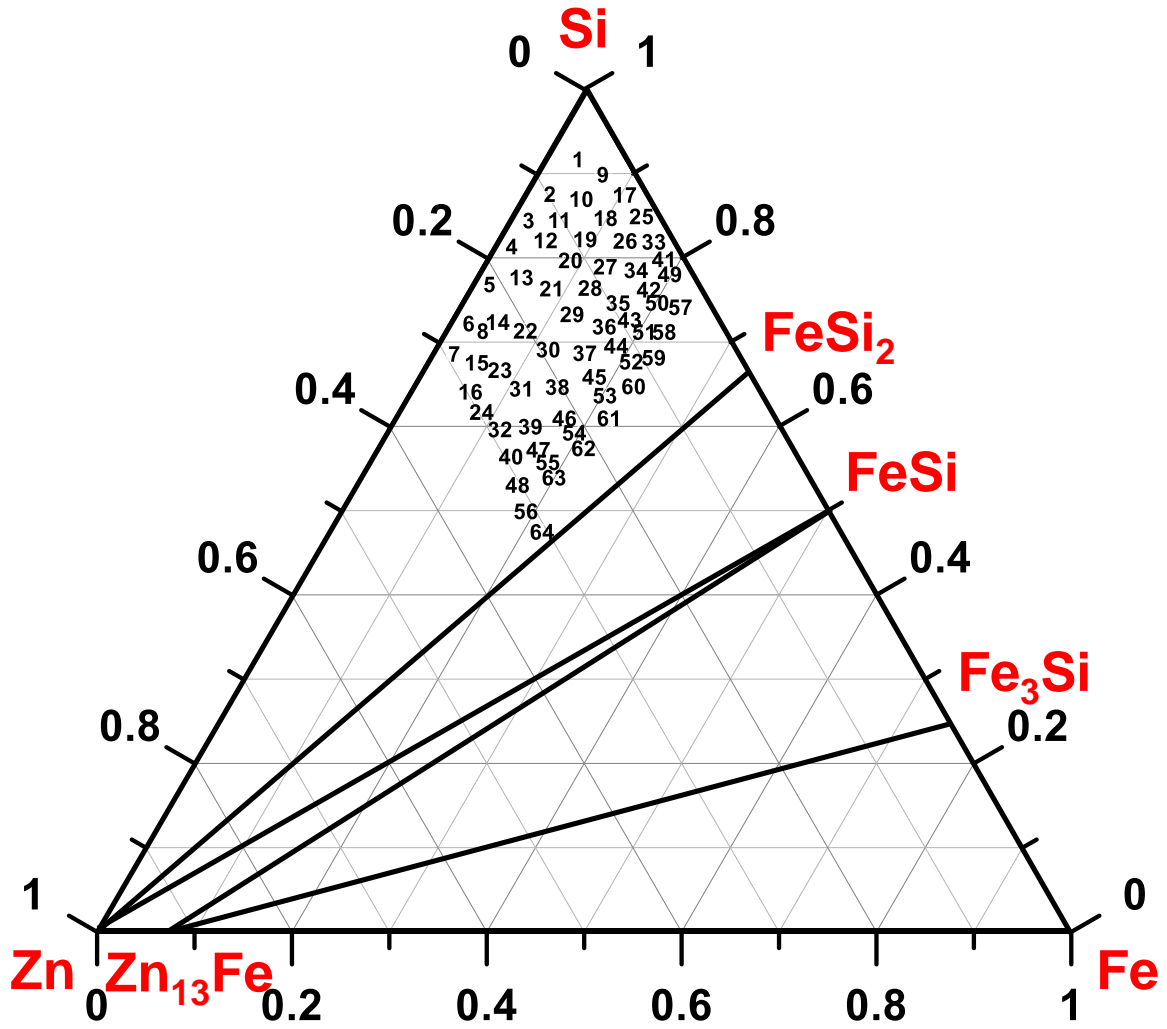
372
373
374
375

376   **Figure 2**
377
378
379

380
381

382
383 **Figure 3**
384
385
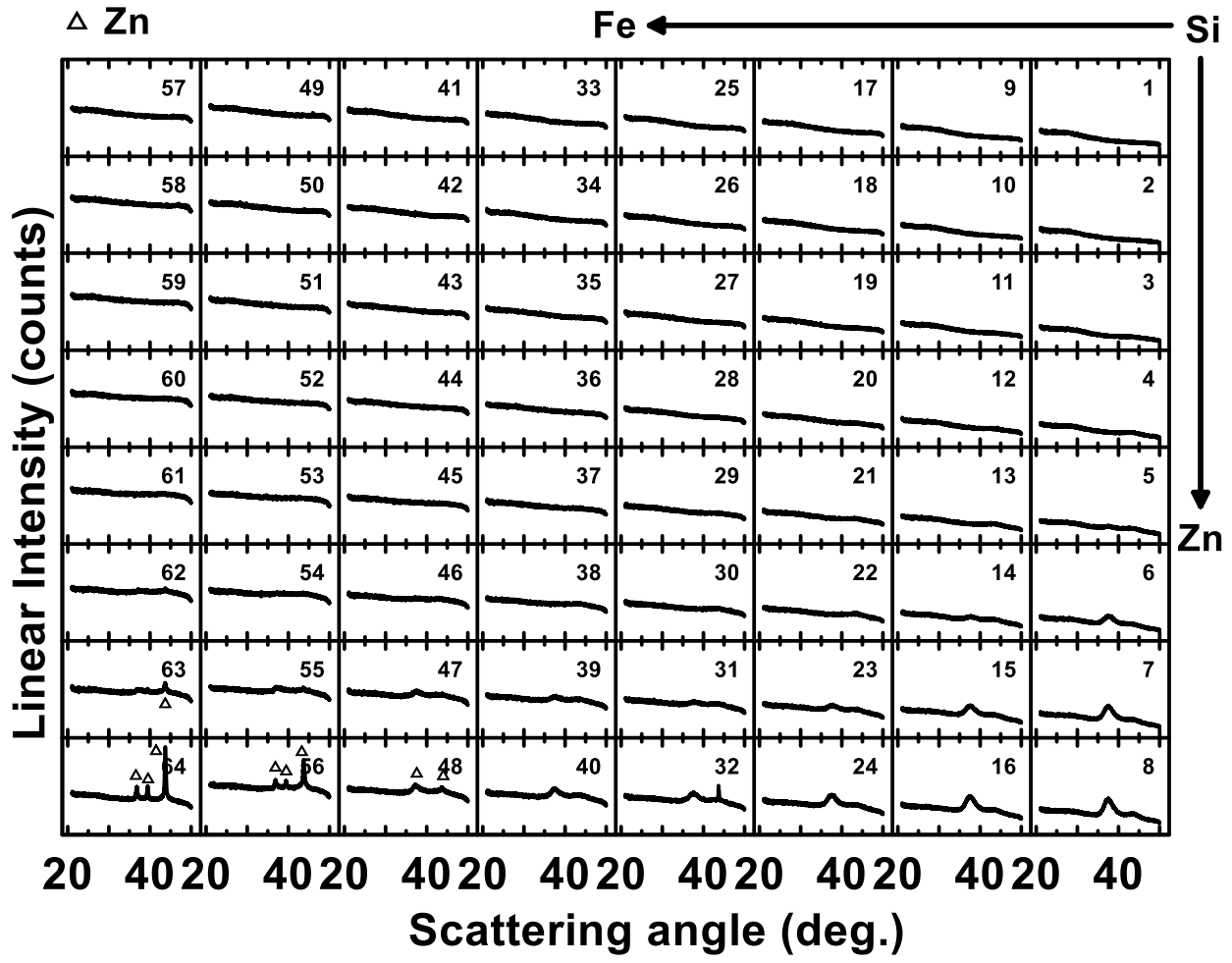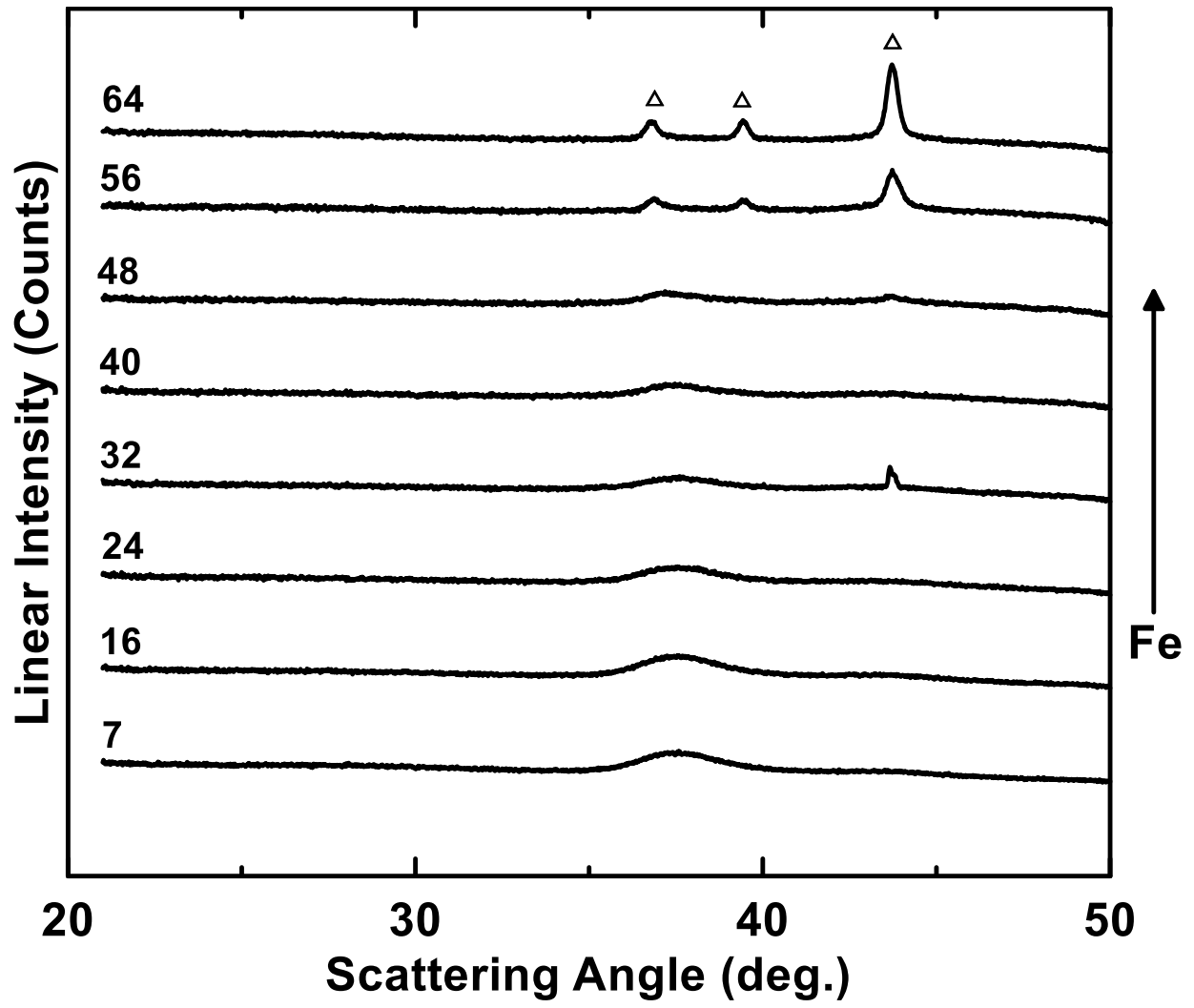
386
387
388
389

390   **Figure 4**
391
392
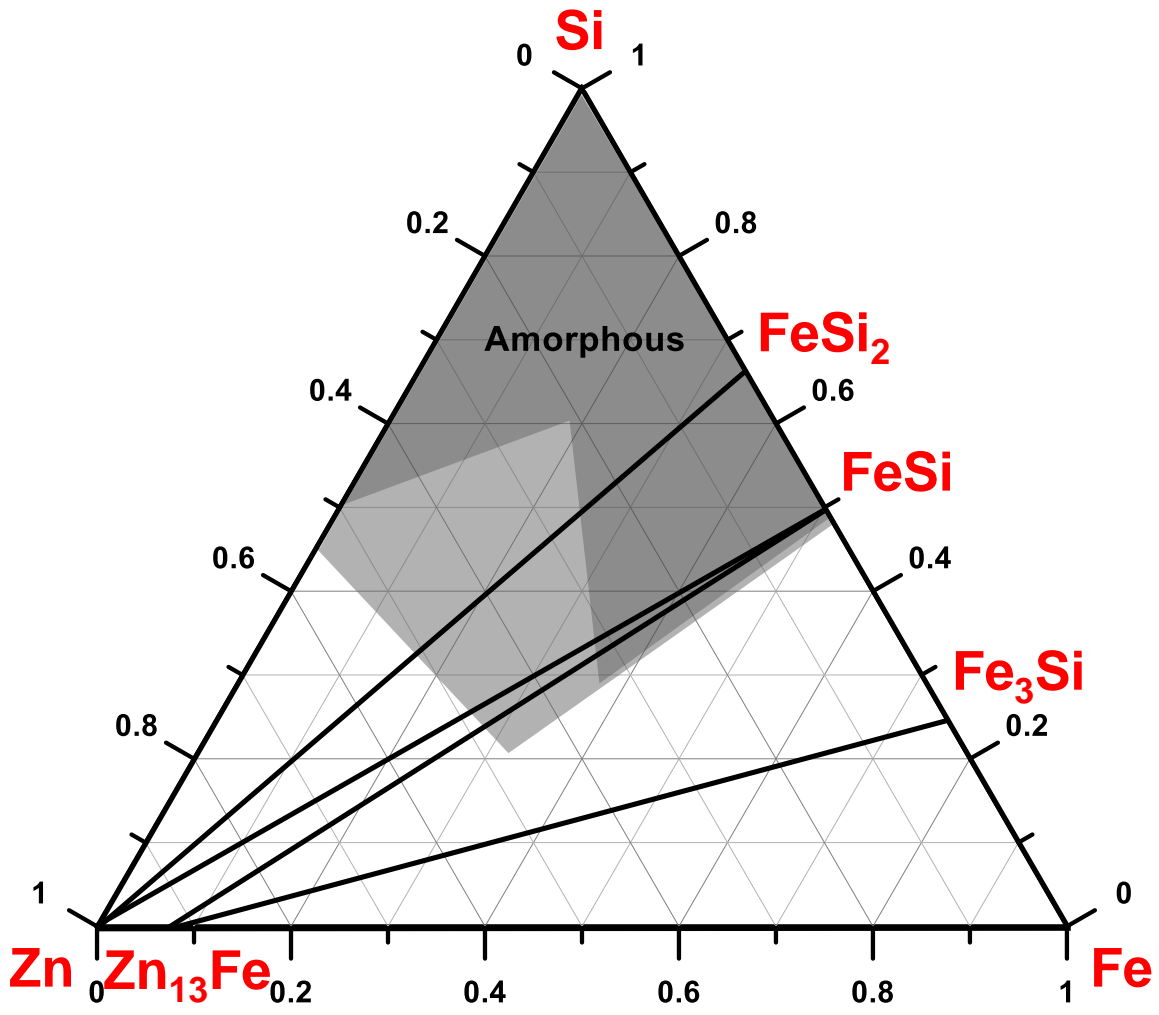
393
394
395
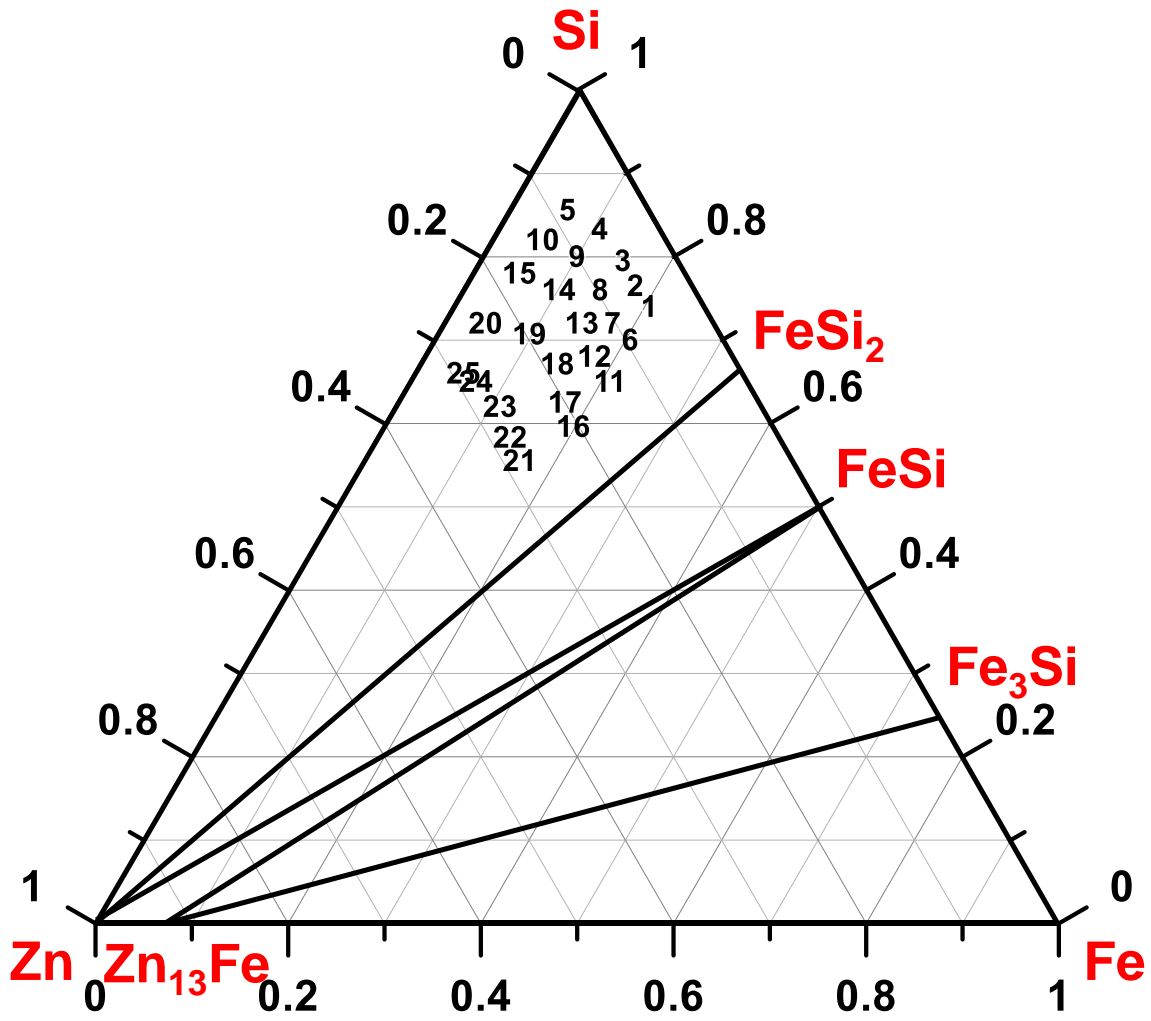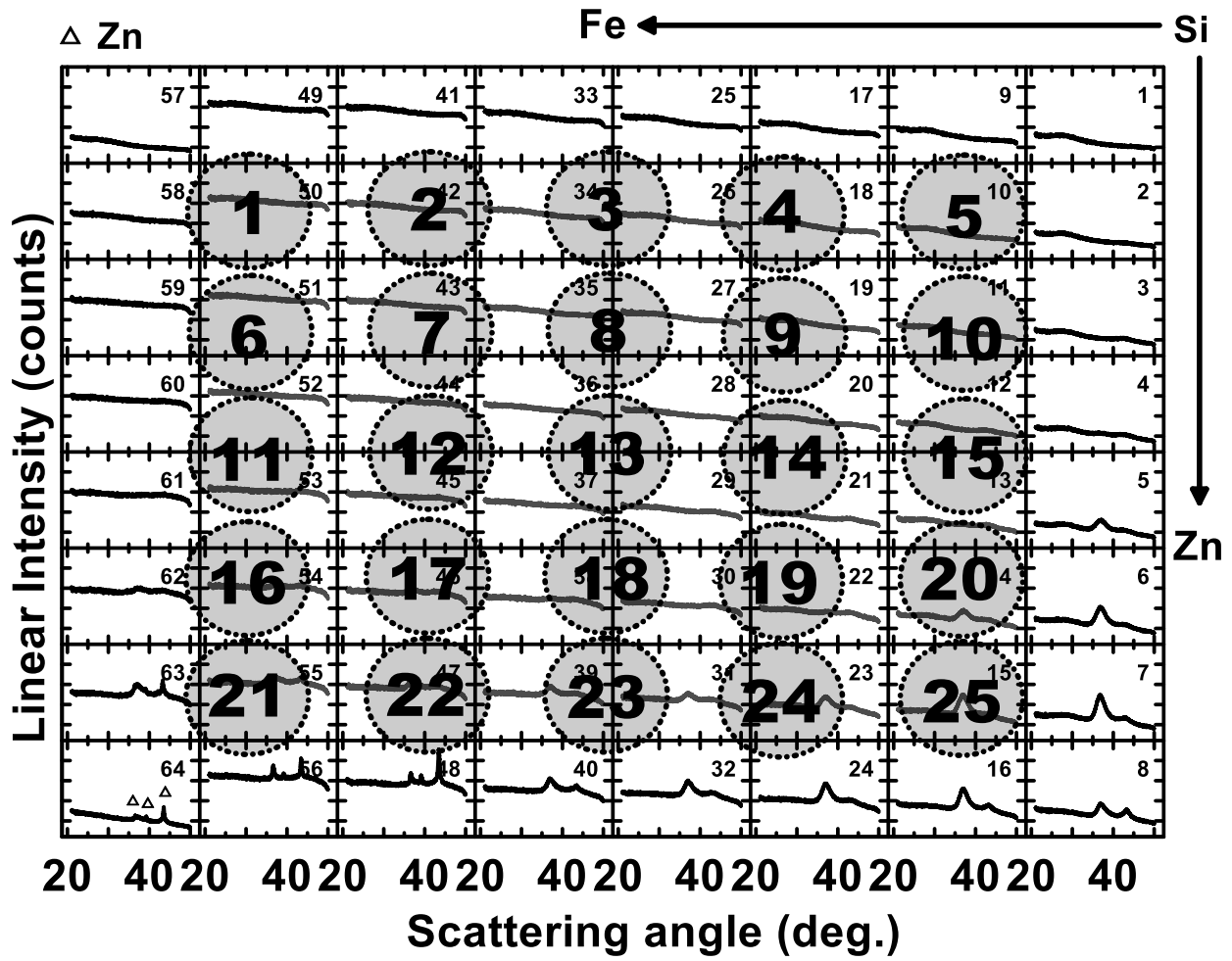
Figure 6

Figure 7

413   **Figure 8**
414
415

Cycle 1-2
Cycle 6-7

Fe ← Si

Zn

Differential Capacity (mAh/gV)

Potential (V)

416
417
418
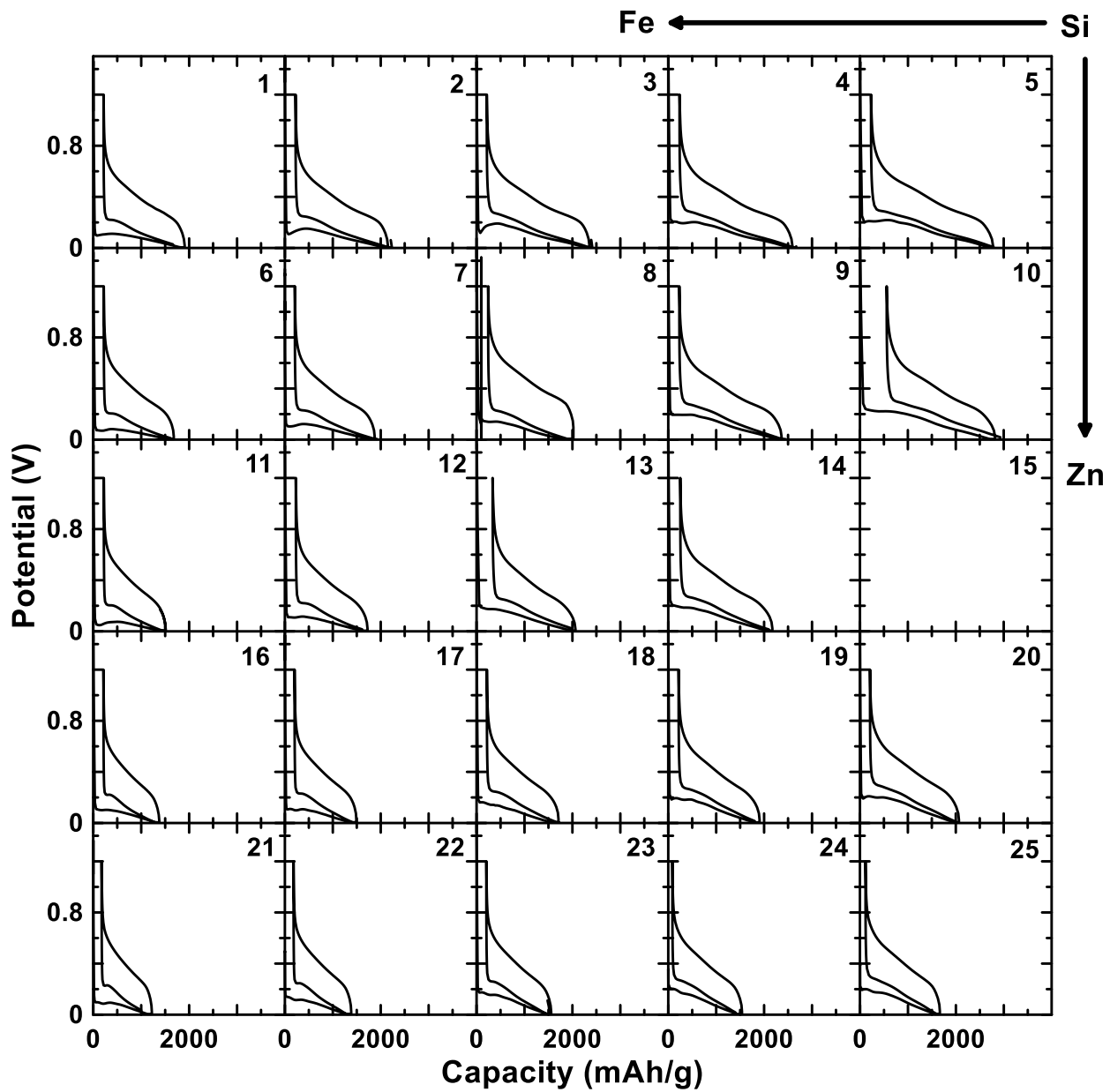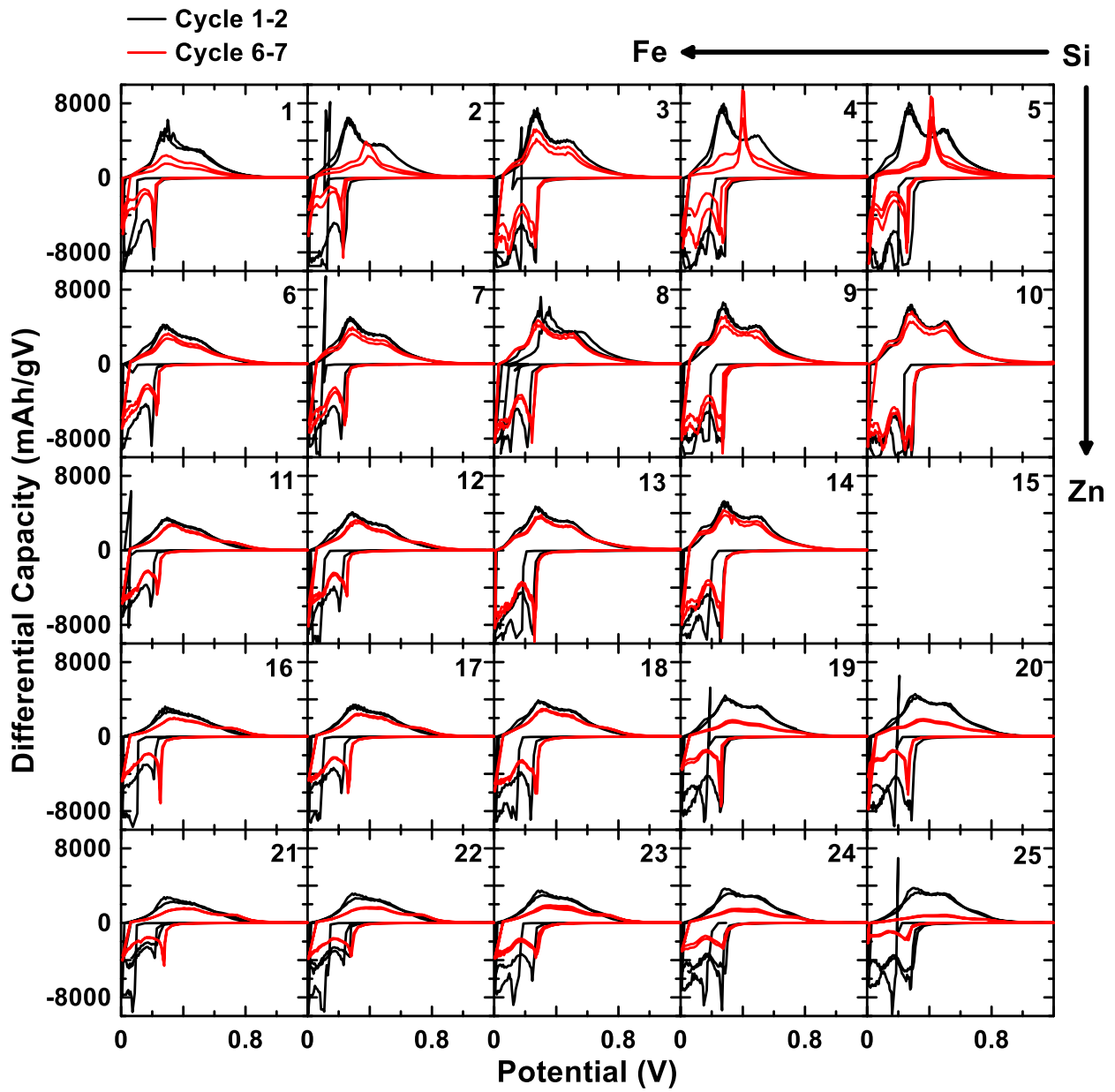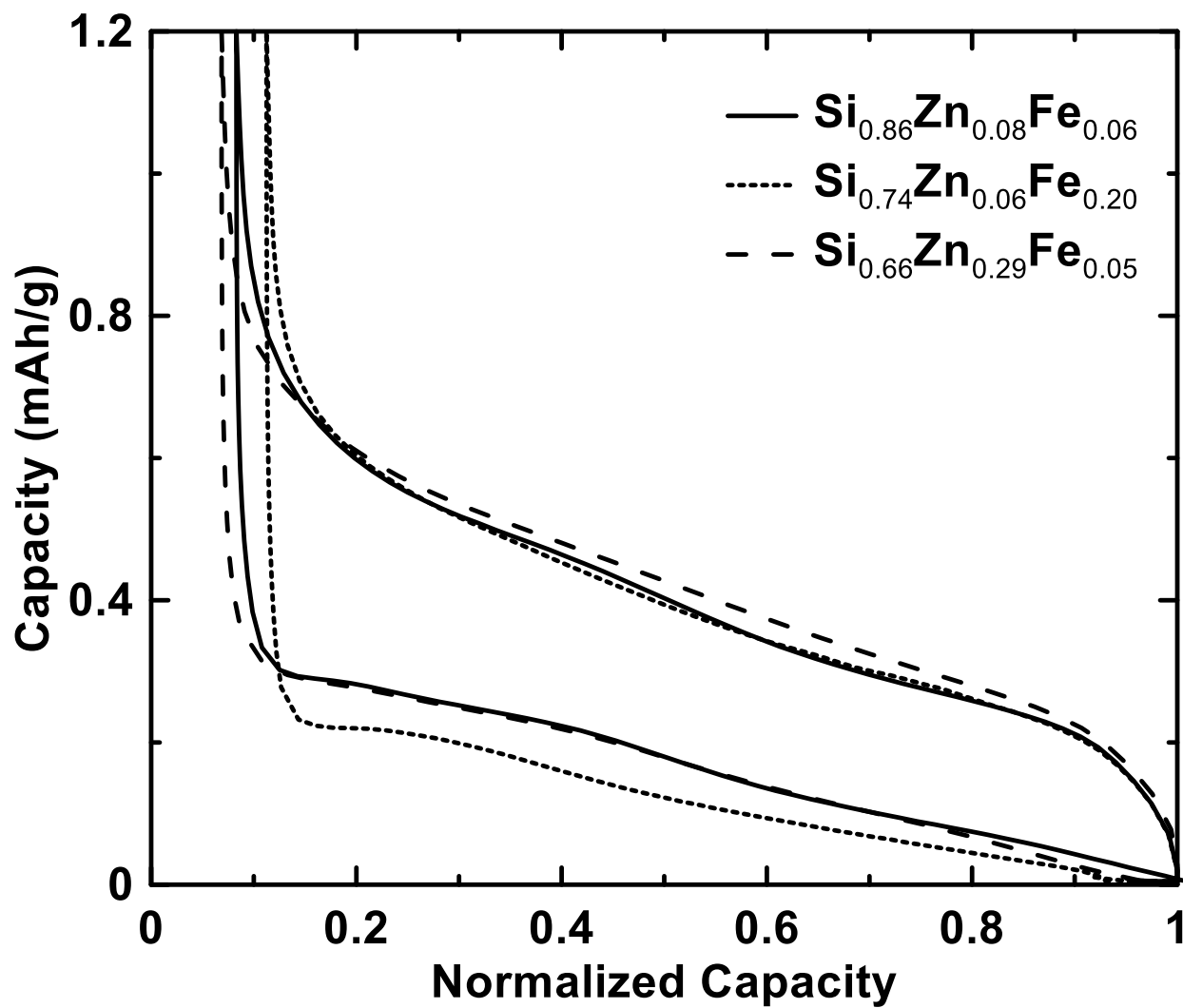
Figure 9

427   **Figure 10**
428
429
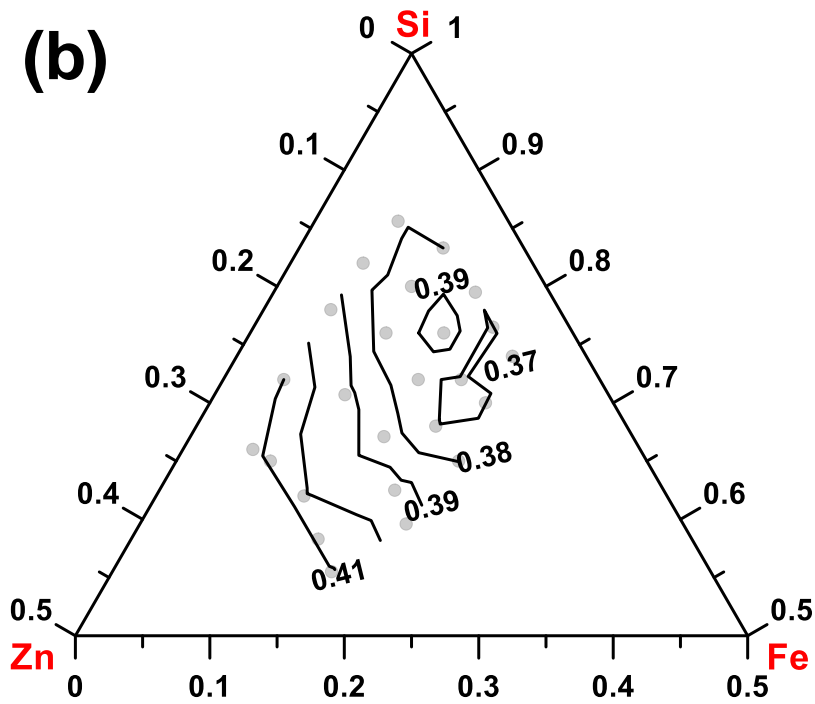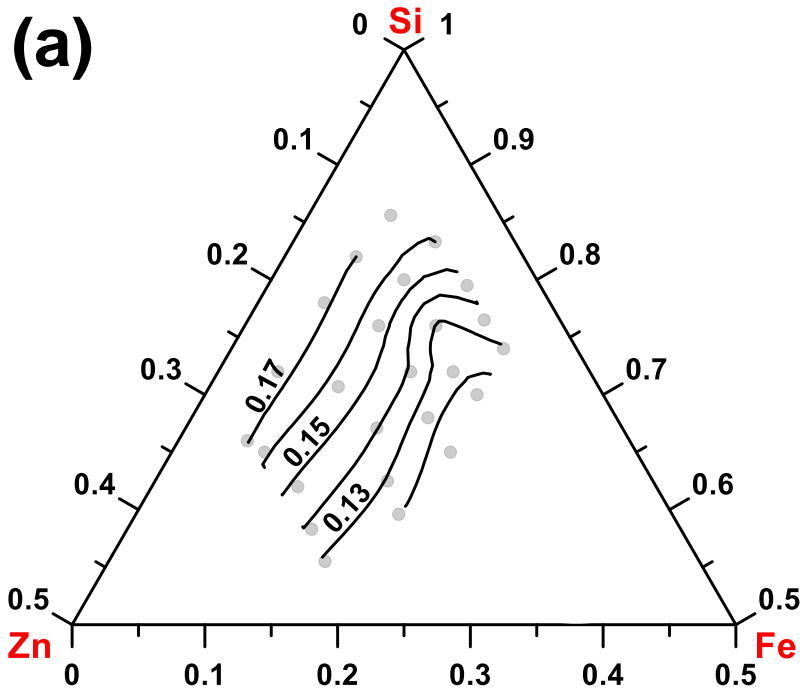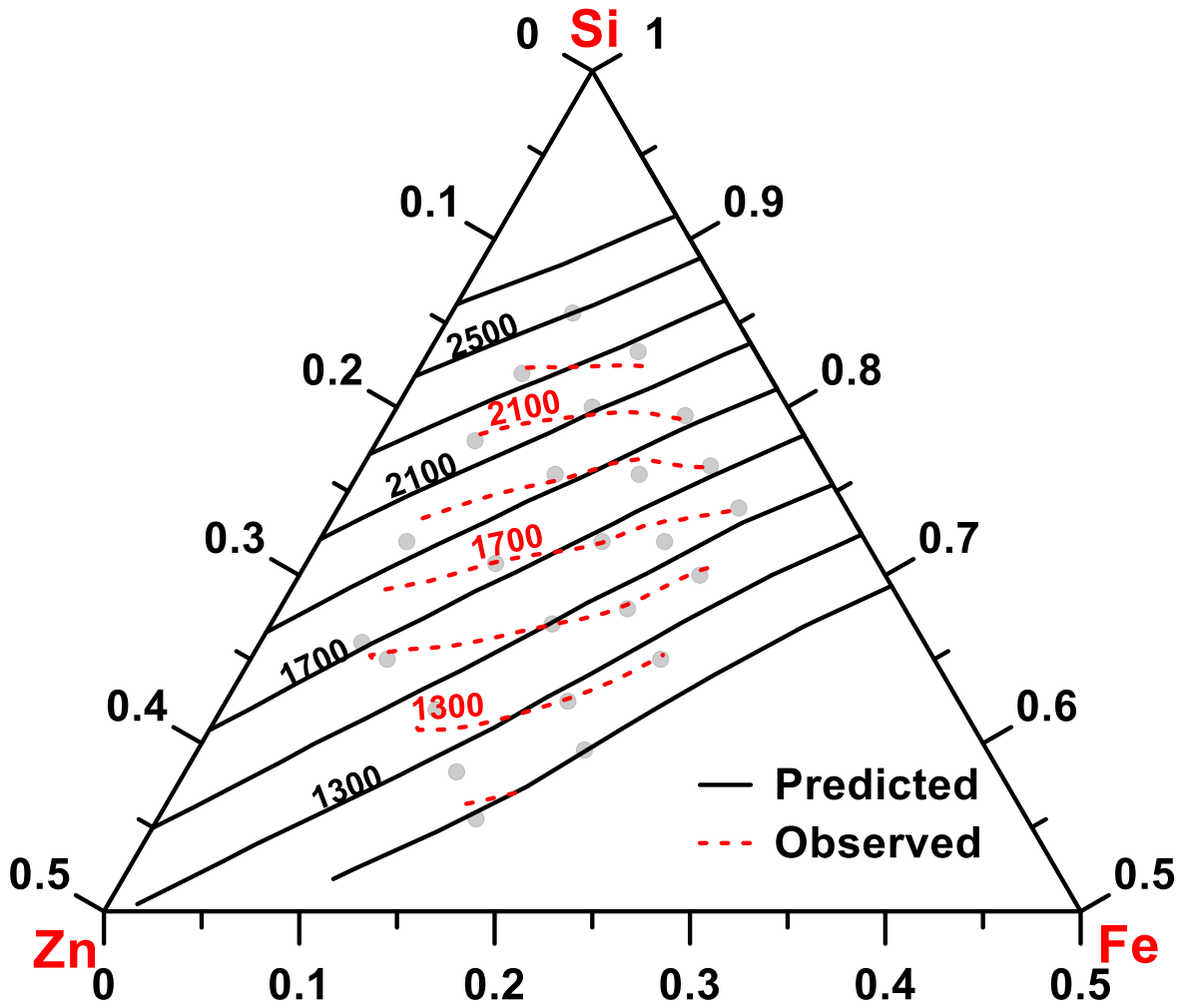

430
431
432
433

434   **Figure 11**

435

436

437

438

439

Figure 12